Exp Fluids (2014) 55:1665
DOI 10.1007/s00348-014-1665-0

RESEARCH ARTICLE

Free-stream density perturbations in a reflected-shock tunnel

N. J. Parziale · J. E. Shepherd · H. G. Hornung

Received: 28 August 2013 / Revised: 18 December 2013 / Accepted: 4 January 2014 / Published online: 16 January 2014

Abstract Focused laser differential interferometry is used to quantify the free-stream density perturbations in the T5 reflected-shock tunnel. The investigation of reflected-shock tunnel disturbances is motivated by the study of hypervelocity boundary-layer instability and transition. Past work on hypersonic wind-tunnel noise is briefly reviewed. New results are reported for hypervelocity air flows at reservoir enthalpies between 5 and 18 MJ/kg at Mach $\approx$ 5.5. Statistical analysis finds no correlation of RMS density perturbations with tunnel run parameters (reservoir pressure, reservoir mass-specific enthalpy, free-stream unit Reynolds number, free-stream Mach number, and shot number). Spectrograms show that the free-stream disturbance level is constant throughout the test time. Power spectral density estimates of each of the experiments are found to collapse upon each other when the streamwise disturbance convection velocity is used to eliminate the time scale. Furthermore, the disturbance level depends strongly on wavelength. If the disturbance wavelength range of interest is between 700 μm and 10 mm, the tunnel noise is measured to be less than 0.5 % with the focused laser differential interferometer.

This work is based in part on the Ph.D. dissertation of the first author (Parziale 2013); additionally, it was an activity that was part of National Center for Hypersonic Laminar–Turbulent Research, sponsored by the "Integrated Theoretical, Computational, and Experimental Studies for Transition Estimation and Control" project supported by the US Air Force Office of Scientific Research and the National Aeronautics and Space Administration (FA9552-09-1-0341).

N. J. Parziale (✉) · J. E. Shepherd · H. G. Hornung
California Institute of Technology, 1200 E. California Blvd., MC 205 45, Pasadena, CA, USA
e-mail: nick.parziale@gmail.com

Present Address:
N. J. Parziale
Stevens Institute of Technology, 1 Castle Point on Hudson, Hoboken, NJ 07030-5991, USA

1 Introduction

Boundary-layer receptivity is an important component of the boundary-layer instability and transition problem. This makes the characterization of the noise environment in the free-stream of any wind tunnel a key aspect of studying transition in ground test (Morkovin 1969; Reshotko 1976; Saric et al. 2002; Fedorov 2003, 2011; Balakumar and Kegerise 2010). Extensive reviews of the effect of tunnel noise on high-speed boundary-layer transition have been made by Schneider (2001, 2004).

The free-stream disturbances in a supersonic wind tunnel include acoustic waves, entropy inhomogeneity, and vortical perturbations, in addition to microscale and macroscale particulates (Bushnell 1990). The major sources of these disturbances within the test region of a reflected-shock tunnel, as shown in Fig. 1, are identified as the turbulent boundary layer on the nozzle wall, and the entropy fluctuations being advected from the reservoir of the facility (Schneider 2001).

Researchers have found some correlation of the tunnel-noise environment to the boundary-layer transition location (Pate and Schueler 1969; Pate 1971a, b, 1974, 1980; Wagner et al. 1970; Stainback and Wagner 1972; Owen et al. 1975). The study of tunnel noise effects on boundary-layer instability has led to the development of hypersonic wind tunnels with low disturbance levels (Blanchard et al. 1996; Schneider 2008; Hofferth et al. 2013). This is achieved by reducing the entropy inhomogeneity and

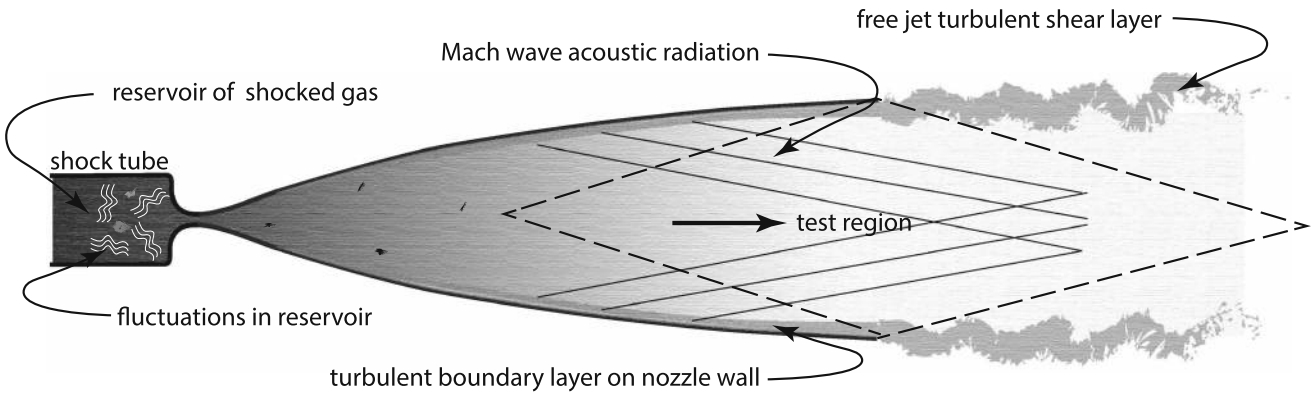

Fig. 1 Schematic of reflected-shock tunnel nozzle used in T5 to create the test gas flow. The *dashed line* represents the approximate border of the test region. The major sources of noise in a reflected-shock tunnel are sound radiation from the turbulent boundary layer on the nozzle, the free jet turbulent shear layer at the exit of the nozzle, and fluctuations in entropy, pressure, and vorticity generated by the shock reflection process used to generate the high-enthalpy reservoir at the end of the shock tube just upstream of the converging–diverging nozzle

ensuring that the nozzle-wall boundary layer is laminar. Hypersonic instability and transition work has been successful in these low-disturbance wind tunnels; however, they are not able to produce hypervelocity flows (>2.5 km/s) where fluid-dynamic/thermo-chemical interactions can exist. It is therefore essential to characterize the noise of the test facility in a study of hypervelocity boundary-layer instability.

Pitot pressure measurement is often used to quantify the perturbations in the test gas of high-speed wind tunnels (Bounitch et al. 2011; Rufer and Berridge 2012). Pitot pressure measurements of the noise in a reflected-shock tunnel are difficult because (1) the bandwidth of commercially available piezoelectric pressure transducers is too low (<1 MHz) to cover the frequency band of importance for slender-body hypervelocity boundary-layer instability study in a high-enthalpy reflected-shock tunnel (10 kHz–10 MHz); (2) the pressure transducers must be flush mounted to avoid resonances in any sort of protective cavity (McGilvray et al. 2009). Flush mounting the transducer causes excessive thermal loading and puts it at risk for particulate impact after the passage of the test gas; and (3) it is uncertain that flush mounted pressure transducers in a Pitot probe configuration produce a faithful representation of the noise level in a supersonic or hypersonic free-stream. The interaction of free-stream fluctuations with the bow-shock wave that forms in front of the transducer may thwart the goal of resolving a wide range of disturbance length scales (Maheash et al. 1995). This interaction is known to be a function of the obliqueness (Moore 1954) and the strength (Lee et al. 1997) of the shock wave. The complexity of the subsonic flow field behind the bow-shock wave may further obscure the fidelity of free-stream disturbance measurement, especially in the frequency domain. Fujii et al. (2013) discuss the oscillation of bow-shock waves at high speeds, and find "that the bow-shock oscillation causes pressure fluctuation in the stagnation region whose magnitude and frequency characteristics strongly depend on the shock stand-off distance".

Hot-wire anemometry (HWA) has also been used to quantify the disturbances in supersonic and hypersonic wind tunnels. Laufer (1961, 1964) used HWA to assess the noise in the JPL 20 inch supersonic wind tunnel. Several key results of this work were (1) that the pressure field radiated by a turbulent boundary layer in a supersonic wind tunnel is consistent with the "Mach wave radiation model" introduced by Phillips (1960) and further developed by Ffowcs-Williams and Maidanik (1965); (2) "[t]he non-dimensional pressure intensity[1] $(\overline{p'^2}/\tau_w^2)$ increases with Mach number"; and (3) the radiated intensity is markedly smaller than that measured at the wall, and the spectrum of the disturbances shifts, so that "the radiated pressure spectrum contains significantly less high-wavenumber components than the pressure spectrum at the wall". Work performed by Stainback and Wagner (1972) note the difficulty of separating the desired flow variables with the "quasi-steady" approach of HWA data reduction. Smits et al. (1983) and Smith and Smits (1993) further developed the HWA technique so that it could be used to measure the flow variables of interest with different wire-heating strategies. These techniques were used by Spina and McGinley (1994) and Weiss et al. (2003) to make successful HWA measurements in supersonic and hypersonic flows. However, the HWA technique cannot be used to study the free-stream noise environment in a high-enthalpy reflected-shock tunnel because (1) the HWA is bandwidth limited (<1 MHz); (2) the total temperature is high in a

[1] Here, p' is the pressure fluctuation derived from the HWA signal and τ_w is the wall shear stress.

high-enthalpy reflected-shock tunnel, making the HWA data reduction strategy of Smits et al. (1983) difficult; and (3) the flow during the starting process and after the test time is impulsive and harsh; this would likely compromise the HWA wires.

Non-intrusive optical methods are an alternative to direct measurements. One approach described by Marineau and Hornung (2010) was to track the unsteadiness of the bow-shock wave in front of a blunt body in the T5 test section. Using an edge detection algorithm with high-speed schlieren cinematography, they were able to track bow-shock motion in the 10 kHz range. This frequency response is not adequate for applications to slender-body hypervelocity boundary-layer instability work, where time scales in excess of 5 MHz must be resolved. The single point focused schlieren deflectometry approach described in Parziale et al. (2011) is capable of very high-frequency response (>10 MHz), but is not quantitative. Further refinement, reported in Parziale et al. (2013), resulted in the development of the focused laser differential interferometer (FLDI), which is quantitative and enabled the measurements reported in the present paper.

In the present paper, the FLDI is briefly described, results from a test campaign to measure the free-stream density perturbations in the T5 reflected-shock tunnel are presented, and these results are analyzed.

2 FLDI diagnostic

The FLDI is an appropriate diagnostic for making high-speed wind-tunnel noise measurements because of its high-frequency response (>10 MHz), adequate spatial resolution (700 μm in the streamwise direction, 20 mm in the spanwise direction), and the ability to repeatedly produce quantitative measurements of density fluctuation. The FLDI technique was first described by Smeets (1972) and Smeets and George (1973) for characterizing turbulent jets in a desktop experiment. Parziale et al. (2013) and Parziale (2013) then used the FLDI technique to make measurements of the acoustic instability on a slender body at hypervelocity conditions.

2.1 Description of FLDI setup

The laser used in this experiment is a Spectra-Physics Excelsior diode-pumped solid-state continuous-wave laser (532 nm wavelength, 200 mW power). The high-quality beam (TEM_{00}) does not require additional beam conditioning for use as an interferometer. Following the optical path in Fig. 2, starting from the laser (L), the beam is turned by a periscope arrangement for precise directional control. The beam is expanded by a lens, C_1 (10 mm focal length), and

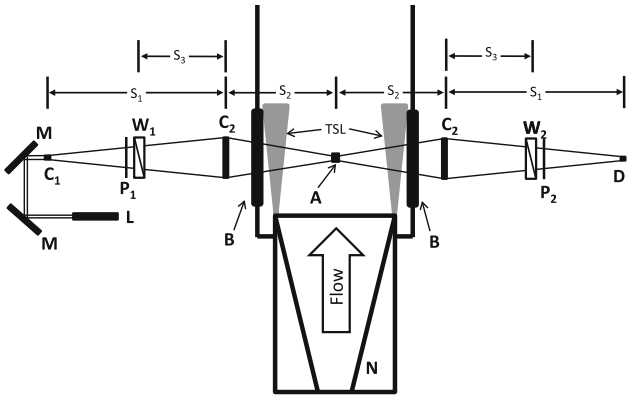

Fig. 2 Annotated schematic of the FLDI. TSL, turbulent shear layer; *L* Laser, *M* mirror, C_1, 10 mm focal length lens; C_2, 300 mm focal length lens, *P* polarizer, *W* Wollaston prism, *B* BK7 window, *A* probe volume, *D* photodetector, *N* nozzle, $s_1 = 718$ mm, $s_2 = 515$ mm, $s_3 = 300$ mm

linearly polarized by P_1 at 45° to the plane of separation of the first Wollaston prism, W_1 (united crystals). The plane of separation of W_1 is chosen to be parallel to streamlines in the free-stream of the contoured nozzle exit. The prism splits the light by a narrow angle (2 arc min) into orthogonally polarized beams. The separation of the beams is fixed at 350 μm by a lens, C_2 (300 mm focal length), while the diameter of the beams is reduced to small values in the center of the test section. This arrangement creates two beams with orthogonal polarization that traverse much of the same optical path. The orthogonally polarized beams do not share the same optical path within ±10 mm of the focal point (along the beam direction, centered at A in Fig. 2). In this region, the beams are calculated to be less than 100 μm in diameter and traverse separate but very closely spaced volumes; they are 350 μm apart (assuming $1/e^2$ Gaussian beam propagation, Siegman 1986). It is primarily within this small focal region that the diagnostic is sensitive to the difference in optical path length between the two beams. The Nyquist wavelength of this setup is 700 μm, double the beam spacing. Beyond the beam focus, the optical paths are nearly common and an additional lens, C_2 (300 mm focal length), refocuses the beams. The second Wollaston prism, W_2, and polarizer, P_2, recombine and then mix the orthogonally polarized beams, such that the interference will be registered as irradiance fluctuations by the photodetector. The response of the photodetector (22.5 V battery biased FDS100 photodiode, terminated at 50 Ω) is amplified by a gain of 5 (SRS SR445) and digitized at 100 MHz by a 14-bit Ethernet oscilloscope (Cleverscope CS328A-XSE).

The probe volume is located at the centerline of the nozzle (±15 mm) and 110 ± 15 mm from the nozzle exit. The latter distance is required because of the recoil (typically <90 mm) of the reflected-shock tunnel (recoil mass: 40 tonnes).

A relation for the change in density ($\Delta\rho$) normalized by the local density (ρ_L) in terms of the output voltage of the photodetector (V) and several fixed parameters in the experiment can be derived by considering the interference at the detector (D, Fig. 2) of the light from the recombined beams as

$$\frac{\Delta\rho}{\rho_L} = \frac{\lambda_0}{2\pi KL\rho_L}\sin^{-1}\left(\frac{V}{V_0} - 1\right), \quad (1)$$

where λ_0 is the wavelength of the laser, K is the Gladstone–Dale constant, and L is the integration length. Along the integration length, [2] extending approximately 10 mm along the beam path on each side of the focal volume; the beams probe separate but closely space volumes, and it is assumed that the FLDI acts as a two-beam interferometer in this region. The change in density, $\Delta\rho = \rho_{\parallel} - \rho_{\perp}$, is the change in density between the two beams; $\rho_{\parallel}$ is the local density at the laser beam polarized parallel to the streamwise direction and $\rho_{\perp}$ is the local density at the laser beam polarized perpendicular to the spanwise direction.

The interferometer is set to the most linear part of a fringe before each experiment, so there is a $\pi/2$ rad phase shift introduced, and V_0 is the voltage at the most linear part of a fringe. During the experiments, the phase shift, $\Delta\phi$, is less than $\pi/3$ rad, so there is no fringe ambiguity. The error in $\Delta\rho/\rho_L$ is estimated by propagating the error (as in Coleman and Steele (1999)) in each of the inputs in Eq. 1, assuming the errors in the inputs are independent of each other. Further details of the instrumentation setup, characterization, and error analysis can be found in Parziale et al. (2013) and Parziale (2013).

2.2 Sensitivity to wavelength

The sensitivity of the technique to disturbance wavelength due to the experimental setup is discussed in this subsection. The FLDI technique is able to probe only a small volume in a test gas because the sensitive leg and reference leg share much of the same optical path, except near the focus. This provides cancelation of density disturbances that exist in the flow but are not located in the measurement region; for example, the turbulent shear layers that the beams must pass through to optically access the test region. The optical arrangement of the focal volumes results in an instrument response that varies with the wavelength of the density disturbance passing through the focal region.

A sketch of a streamwise slice of the flow field of interest at the probe volume shows the relative location of the laser beams and four sine waves intended to be representative of disturbances in density (Fig. 3). The density disturbances are assumed to have the form $\rho' = Re(\rho_A \exp(i(2\pi s/\lambda - \omega t)))$, with the same amplitude ρ_A, and different wavelengths $\lambda = 0.7, 2, 4, 8$ mm. The streamwise distance is s, the frequency is ω, and time is t. Referencing Fig. 3, at the Nyquist wavelength, the response of the FLDI will be at its maximum, and the change in density registered by the FLDI, $\Delta\rho = \rho_{\parallel} - \rho_{\perp}$, will be the density disturbance amplitude, ρ_A; $\rho_{\parallel}$ is the local density at the laser beam polarized parallel to the streamwise direction, and $\rho_{\perp}$ is the local density at the laser beam polarized perpendicular to the spanwise direction. For wavelengths longer than 700 μm, the observed spatial change in density ($\Delta\rho = \rho_{\parallel} - \rho_{\perp}$) will decrease with increasing wavelength for a disturbance of the same peak amplitude. The relationship $c(\lambda)$ between observed response and actual peak magnitude can be readily derived (Parziale 2013) for sinusoidal disturbances and is

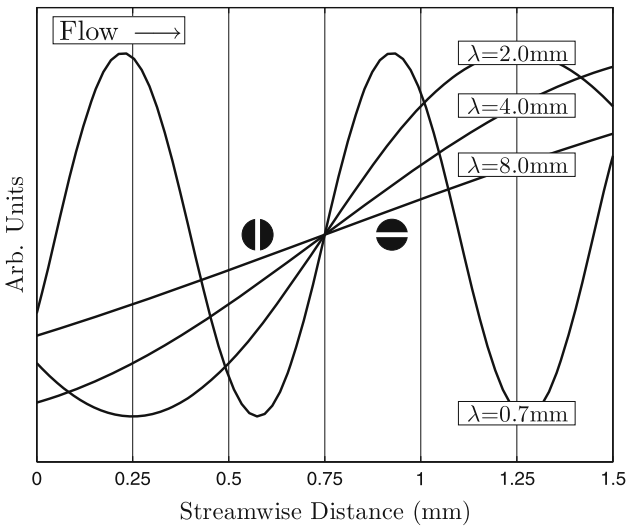

Fig. 3 Streamwise direction is left to right, spanwise direction is in and out of the page. The four sine waves shown are representative of density disturbances of equal amplitude with wavelengths: 0.7, 2, 4, and 8 mm. The *two circles* represent the beam polarized in the streamwise and spanwise direction, denoted by the *horizontal* and *vertical lines* though the *circles*, respectively

$$c(\lambda) = \sin\left(\frac{2\pi l_b/2}{\lambda}\right), \quad (2)$$

where l_b is the beam spacing. The coefficient demonstrates the behavior of reduced response with increasing wavelength (Fig. 4). In order to use the coefficient of Eq. 2 to correct the observations obtained from Eq. 1, the data must be transformed into wavelength–amplitude space; this is done in this work by transforming the data into frequency–amplitude space, using a velocity scale to convert to wavelength, and applying the coefficient as

$$\left(\frac{\Delta\rho(\lambda)}{\rho_L}\right)_{\text{coef}} = \left(\frac{\Delta\rho(\lambda)}{\rho_L}\right)/c(\lambda) \quad (3)$$

[2] The determination of the integration length and its uncertainty are discussed at length in Parziale (2013).

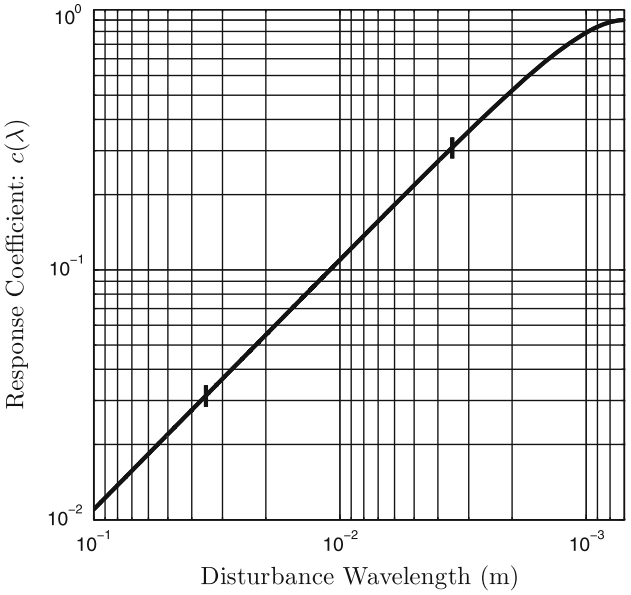

Fig. 4 Plot of the response coefficient as a function of wavelength demonstrating the behavior of reduced response with increasing wavelength. The *error bars* here represent the error in Eq. 2 due to the error beam spacing

where $(\Delta\rho(\lambda)/\rho_L)_{\text{coef}}$ is the response after the coefficient has been applied.

The velocity scale to convert the density perturbations from frequency–amplitude space to wavelength–amplitude space is the streamwise convection velocity (U_S) of the disturbances. We refer to Fig. 6 of Laufer (1964) for the streamwise convection velocity, which was measured by HWA cross-correlation; at Mach 5 $U_S = KU_X = 0.58\ U_X$, where K is the disturbance convection velocity factor. So, the frequency f is converted to wavelength as $\lambda = KU_X/f = 0.58\ U_X/f$. Uncertainty in the choice of the disturbance convection velocity factor will shift the wavelength spectrum and change the RMS density perturbations. There will also be added uncertainty from the application of Eq. 2 from uncertainty in the beam spacing; this is primarily due to misalignment in the distance s_3 and the divergence angle of the Wollaston prism in Fig. 2. The misalignment is assumed to be 5 mm in the distance s_3, and the error in divergence angle is assumed to be 3 arc s. Propagating the error, as in Coleman and Steele (1999), results in an uncertainty of the beam spacing of 350 ± 11 µm. The uncertainty from velocity choice and beam misalignment has a small effect on the measured RMS density fluctuations and will be discussed quantitatively in Sect. 4.

The measurement technique has a preferred direction along the free-stream velocity vector because of the optical arrangement. Inferences on wavelength, such as those shown in Figs. 4 and 8, are restricted in interpretation as the projection of the disturbance wavevector, $\hat{k}$, on the axial direction, $\hat{n}_{\text{ax}}$, as $\lambda = 2\pi/(\hat{k}\cdot\hat{n}_{\text{ax}})$. The fundamental output of the detector is the difference in density between the two beams; this is converted to frequency space, which is unambiguous; however, the projected wavelength is subject to interpretation. In our simplified model of the detector response, we have assumed a plane wave moving in a constant but unknown direction. This is a simplification, as the noise spectrum is the result of a superposition of waves from all acoustic sources in the flow, including the settling chamber (reservoir) as well as the boundary layer.

We expect that disturbances originating within the settling chamber may be propagating with wavefronts perpendicular to the axial direction, $\hat{n}_{\text{ax}}$. However, it is observed (Laufer 1964) and is consistent with the theory of acoustics in supersonic flow (Phillips 1960) that the radiation from the boundary layer is oblique to the flow. Radiation from a stationary point source in supersonic flow is within a cone bounded by the Mach lines. Within the nozzle, the Mach lines vary in angle $\sin\theta = 1/M$ as the mean flow accelerates so that the wave will be refracted when traveling from the boundary layer to the measurement position.

The radiation from a turbulent boundary layer is more complex than a simple stationary source, as the origin is the spatially distributed and rapidly moving large-scale motions in the outer portion of the boundary layer. As a consequence, the radiated acoustic wave front forms an angle, θ, to the free-stream velocity vector. Phillips (1960) bounds this angle as $\cos^2(\theta) > (M(1-K))^{-2}$, where K is the non-dimensional boundary-layer disturbance propagation velocity, and M is the free-stream Mach number. We have not attempted to address the inverse problem of how to relate the measurements, which integrate over all the disturbances in the flow, to the radiation from the boundary layer. This is outside the scope of the present paper. Resolving this issue will require detailed numerical simulation and validation through the further development of the present technique to sense the direction of disturbance propagation.

3 Facility, test procedure, and run conditions

All measurements are made in T5, the free-piston-driven reflected-shock tunnel at the California Institute of Technology (Fig. 5). It is the fifth in a series of shock tunnels designed to simulate high-enthalpy real-gas effects on aerodynamics of vehicles flying at hypervelocity speeds through the atmosphere. More information regarding the capabilities of T5 can be found in Hornung (1992).

An experiment is conducted as follows: a 120 kg aluminum piston is loaded into the compression tube/secondary reservoir junction. A secondary diaphragm (mylar, 127 μm thick) is inserted at the nozzle throat at the end of the shock tube near the test section and a primary diaphragm (stainless steel, 7–10 mm thick) is inserted at the compression tube/shock tube junction. The test section, shock tube, and compression tube are evacuated. The shock tube is filled with the test gas (in the present study, air to 20–150 kPa), the compression tube is filled with a He/Ar mixture to 45–150 kPa, and the secondary reservoir is filled with air to 2–11 MPa. The air in the secondary reservoir is released, driving the piston into the compression tube. This piston motion adiabatically compresses the driver gas of the shock tunnel to the rupture pressure of the primary diaphragm (20–120 MPa). Following the primary diaphragm rupture, a shock wave propagates in the shock tube and is reflected off the end wall, breaking the secondary diaphragm and reprocessing the test gas. The test gas is then at high temperature (2,000–9,000 K) and pressure (15–80 MPa) with negligible velocity, and is then expanded through a converging–diverging contoured nozzle to $M_X \approx 5.5$ in the test section.

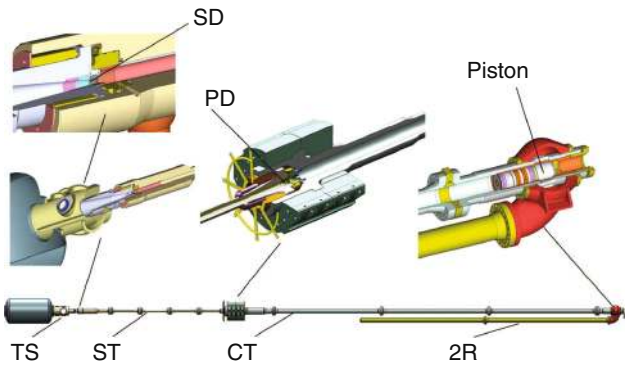

Fig. 5 A schematic of T5 with a blown up view of each of the major sections. *SD* secondary diaphragm, *PD* primary diaphragm, *TS* test section, *ST* shock tube, *CT* compression tube, *2R* secondary reservoir

Initial shock tube pressure P_1, measured primary shock speed U_S, and reservoir pressure P_R are used to compute the reservoir conditions for each shot. The primary shock speed and initial shock tube pressure are used to calculate the thermodynamic state of the gas after being processed by the primary and reflected-shock waves, assuming thermo-chemical equilibrium. The gas pressure behind the reflected-shock wave is changed isentropically, assuming chemical-thermodynamic equilibrium, to the measured reservoir pressure (P_R) to account for the weak expansion or compression waves that are reflected between the contact surface and the shock tube end. Thermo-chemical calculations are performed using Cantera (Goodwin 2003) with the Shock and Detonation Toolbox (Browne et al. 2006). The appropriate thermodynamic data are found in the literature (Gordon and McBride 1999; McBride et al. 2002).

The steady expansion through the contoured nozzle (area ratio: 100) from the reservoir to the free-stream is modeled by the axisymmetric, reacting Navier–Stokes equations as described in by Candler (2005), Johnson (2000), and Wagnild (2012). The translational and rotational degrees of freedom are assumed to be in equilibrium. The vibrational degree of freedom is allowed to deviate from equilibrium. The boundary layer on the nozzle wall is assumed to be turbulent and modeled by one equation as in Spalart and Allmaras (1992) with the Catrisa and Aupoix (2000) compressibility correction. The grid is generated by the commercial tool, Gridgen.

4 Results and discussion

A test series using the FLDI measurement technique for a series of seven shots (conditions in Table 1) was executed to investigate the noise in the free-stream flow of T5. The

Table 1 Run conditions

Shot (#)	P_R (MPa)	h_R (MJ/kg)	T_R (K)	U_X (m/s)	ρ_X (kg/m^3)	P_X (kPa)	T_{trX} (K)	T_{vX} (K)	M_X (−)	Re_X^{Unit} (1/m)
2684	46.6	8.0	5,331	3,677	0.059	18.9	1,113	1,116	5.47	4.9E+6
2686	49.5	13.9	7,591	4,629	0.041	24.6	2,014	2,016	5.00	2.9E+6
2687	49.3	15.9	8,141	4,891	0.036	25.0	2,248	2,250	4.94	2.5E+6
2691	41.8	5.5	4,200	3,114	0.071	14.1	683	694	5.93	6.7E+6
2692	42.4	5.3	4,081	3,053	0.075	14.0	646	657	5.98	7.2E+6
2693	49.6	8.6	5,583	3,790	0.059	20.9	1,216	1,218	5.39	4.8E+6
2694	49.9	17.8	8,570	5,118	0.034	25.8	2,451	2,453	4.90	2.3E+6

Shot is the experiment number; P_R, h_R, and T_R are the pressure, mass-specific enthalpy, and temperature of the reservoir, respectively; U_X, ρ_X, and P_X are the velocity, density, and pressure in the free-stream, respectively; T_{trX} and T_{vX} are the temperatures associated with the translational/rotational and vibrational degrees of freedom in the free-stream, respectively; M_X and Re_X^{Unit} are the free-stream Mach and unit Reynolds numbers, respectively

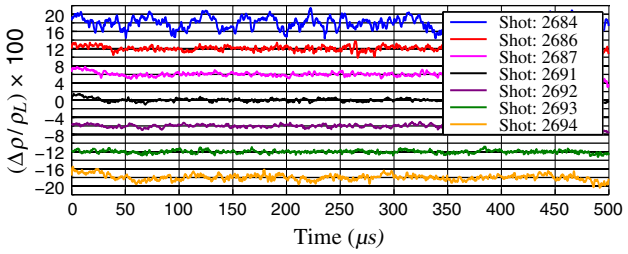

Fig. 6 Filtered time traces of $\Delta\rho/\rho_L \times 100$ (filter cutoffs: 5 kHz–20 MHz). Each trace is offset 6 % along the ordinate and is 500 µs of the steady test time. Note that shot 2684 has a notably larger amplitude than the other shots. Run conditions in Table 1.

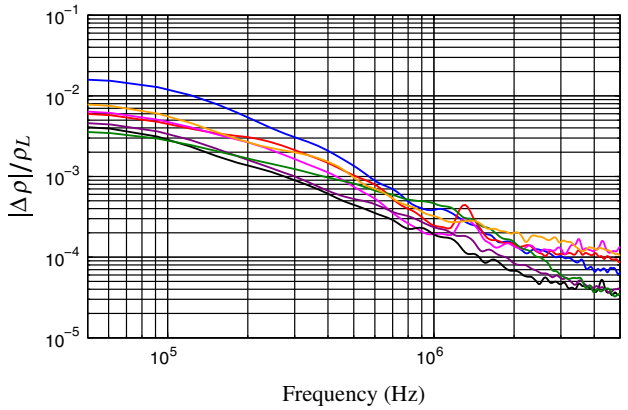

Fig. 7 Frequency spectrum of tunnel noise time traces. Legend in Fig. 6. Run conditions in Table 1. The four RF spikes at 1.3, 1.4, 3.5, and 6 MHz should be disregarded; these peaks also appear when the tunnel is not in operation

test matrix was designed to hold the reservoir pressure (P_R) constant while varying the reservoir enthalpy (h_R) through the useful range of conditions in T5.

Seven bandpass-filtered (5 kHz–20 MHz) time traces of density perturbations (Fig. 6) illustrate that the noise level is similar through the range of reservoir enthalpy h_R, other than shot 2684, which has a larger RMS than the other experiments. This is explained by understanding the process of running T5. Polyurethane buffers slow the piston to a stop after the primary diaphragm is ruptured (refer to Fig. 5), and these buffers were destroyed during the prior experiment (shot 2683). The destroyed buffers introduced material to the shock tube which was not completely removed during the normal cleaning process that is executed after each experiment. During the startup process of shot 2684, this buffer material was introduced to the flow and registered as large fluctuations by the interferometer.

The spectrum[3] of the time traces (Fig. 7) further illustrates the similarity for all tests other than shot 2684.

[3] The data are digitized at 100 MHz. The spectral content of the single-side amplitude is estimated using the discrete Fourier transform with 50 % overlapping 50 kHz Hann windows.

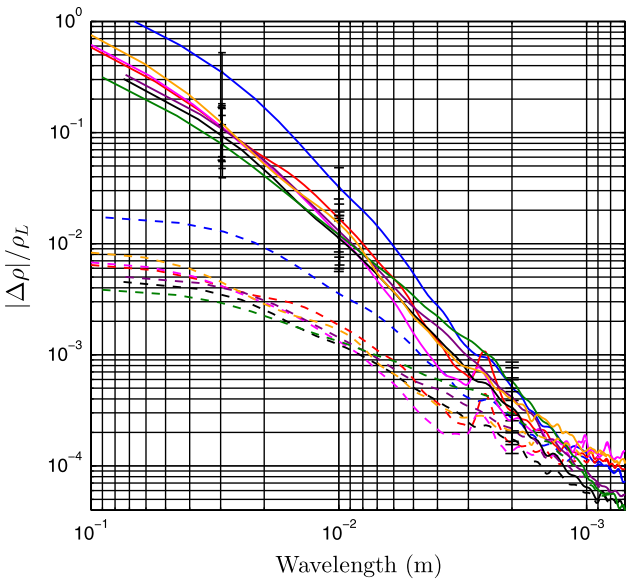

Fig. 8 Wavelength spectrum of tunnel noise time traces. Legend in Fig. 6. Run conditions in Table 1. There are two sets of wavelength spectrum plots of the same data. The lower amplitude data has not been corrected for the sensitivity of the FLDI technique to wavelength (*dashed lines*). The higher amplitude data has been corrected for the sensitivity of the FLDI technique to wavelength (*solid lines*). The size of the error bars was determined by combining the error in Eq. 1 (as in Sect. 2) and the error from approximating the spectral content of the signal. The peaks between 2 and 3 mm are RF spikes that are registered when the tunnel is not in operation, see Fig. 7

Taylor's hypothesis is used to convert the frequency f to wavelength as $\lambda = KU_X/f = 0.58\ U_X/f$, where the disturbance convection velocity factor ($K = 0.58$) is taken from Laufer (1964), and U_X is the free-stream velocity at the nozzle exit (Table 1). This allows the data to be presented in amplitude–wavelength space as in Fig. 8 (dashed lines). Additionally, the wavelength spectrum is corrected for the sensitivity of the FLDI technique to wavelength, as discussed in Sect. 2.2 (Fig. 8, solid lines). There is a clear separation between shot 2684 and the other shots, and the spectra for shots other than 2684 collapse within the uncertainty limits.

Uncertainty in the choice of the streamwise disturbance convection velocity factor (K) will change the RMS density perturbations, though the sensitivity to the factor is not high. For example, decreasing the disturbance convection velocity factor by 25 % will increase the RMS fluctuations by 7 % and increasing the factor by 25 % will decrease the RMS fluctuations by 8 %. The calculated uncertainty in the beam spacing (350 ± 11 µm) changes the RMS fluctuations by no more than 3 %.

Further interpretation of the results in Fig. 8 are given in Table 2. RMS density fluctuations are tabulated at different bandpass wavelengths for each experiment after the response coefficient (Eq. 3) has been applied. Shots 2691

Table 2 Summary of RMS density fluctuations at different bandpass wavelengths

Cutoff		Shot#						
Short (μm)	Long (mm)	2684	2686	2687	2691	2692	2693	2694
700	100	6.70	2.72	2.78	1.69	1.89	1.57	3.33
700	50	4.78	1.89	1.84	1.21	1.38	1.16	2.09
700	25	2.57	1.17	0.99	0.68	0.81	0.73	1.04
700	10	0.72	0.45	0.32	0.26	0.30	0.36	0.41

Run conditions in Table 1. The quantity rms $(\rho/\rho_L) \times 100$ is tabulated for each shot

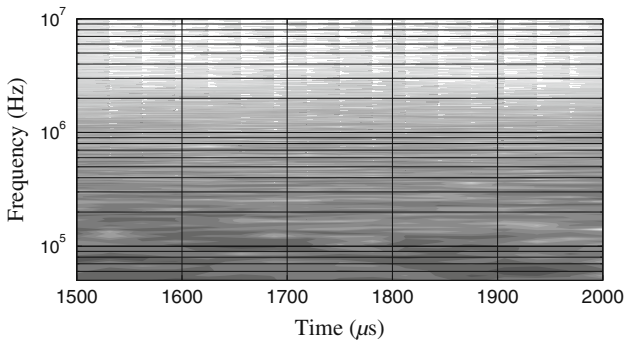

Fig. 9 Spectrogram (contours of power spectral density plotted in time–frequency space) of shot 2693; this illustrates how the spectral content of the fluctuations in the free-stream evolve throughout the test time. It is seen that there are no clear trends in frequency–time space. *Darker shading* indicates larger values of power spectral density (10 $\log_{10}$(|PSD|))

and 2692 were performed at the same nominal condition; the difference in the RMS noise is similar and within experimental error for each pass band presented. It is desirable to understand the amplitude of the RMS density fluctuations at length scales of relevance to slender-body hypervelocity boundary-layer instability and transition work being conducted in T5. So, comparing the scaling of the most amplified wavelength (λ_A) in the boundary layer on a 5° half-angle cone, ($\lambda_A \approx 2\ \delta \approx$ 2–4 mm, Fedorov (2011)) to the measured frequency content of free-stream disturbance is a logical step. For wavelengths near the slender-body hypervelocity boundary-layer instability (700 μm–10 mm), the RMS tunnel noise is not more than 0.5 % (Table 2).

Examination of the spectral content evolution of fluctuations throughout the test time is important because there are complex non-steady wave systems in the reservoir of a reflected-shock tunnel during the starting process and steady run time. The concern is that weak non-steady waves or driver gas contamination (Sudani and Hornung 1998) may manifest themselves during the test time as trends in noise, i.e., the spectral content will shift because the driver gas (helium/argon) leaks into the useful test flow. This point is addressed by constructing a spectrogram[4] of the data previously presented in Fig. 6. An example (Fig. 9) shows contours of $10\log_{10}$(|PSD|) in time–frequency space. The data indicate no clear trends in noise throughout the test time. The other experiments show a similar lack of trend in noise during the run time of the tunnel.

Evidence of correlation between the tunnel noise and run conditions is sought using forward and reverse stepwise regression. The results from shot 2684 are omitted from this exercise because it is identified as an outlier due to error in executing the experiment. The parameters chosen to seek correlation with the tunnel noise are P_R, h_R, Re_X^{Unit}, M_X, and shot number. All data are centered and then normalized by their standard deviation. The p value to enter or leave the regression model is 0.1. The forward selection analysis begins with no parameters in the regression model, and the reverse selection analysis begins with all parameters in the regression model. No parameters are included in the final regression models found by the forward or reverse selection analysis, which indicates that the data are consistent with the null hypothesis,[5] so no parameters are found to be strongly correlated with tunnel noise.

5 Conclusion

In this work, we quantify the noise in the T5 reflected-shock tunnel. The investigation of reflected-shock tunnel disturbances is motivated by hypervelocity boundary-layer instability and transition research. Past work on hypersonic wind-tunnel noise is briefly reviewed.

We eliminate Pitot pressure measurements and hot-wire anemometry as noise measurement techniques in high-enthalpy reflected-shock tunnels on the basis of reasoned arguments. This motivates the use of the FLDI, which can quantify high-frequency density perturbations non-intrusively. The sensitivity of the FLDI technique to wavelength is identified, and a simple amplitude correction is

[4] A spectrogram is made by estimating the power spectral density (PSD) of 10 kHz Hann windows with a 50 % overlap using the Welch method.

[5] Stepwise regression is the use of an F statistic to test models with and without a potential term at each step. If a term is not currently in the model, the null hypothesis is that the term would have a zero coefficient if added to the model. If there is sufficient evidence to reject the null hypothesis, the term is added to the model. Conversely, if a term is currently in the model, the null hypothesis is that the term has a zero coefficient. If there is insufficient evidence to reject the null hypothesis, the term is removed from the model (MathWorks 2013; Draper and Smith 1998).

presented.

A series of experiments is conducted in the T5 reflected-shock tunnel with air as the test gas. The reservoir pressure is held nearly fixed and the enthalpy is varied over nearly the entire T5 parameter space; this procedure has the effect of varying Reynolds number. One experiment (shot 2684) shows an elevated disturbance level; this is because of improperly running shot 2683 and not cleaning the shock tube after the experiment was completed. This run is identified as an outlier. Forward and reverse stepwise regression for the remaining experiments results in a linear regression model consistent with not including P_R, h_R, Re_X^{Unit}, M_X, and/or shot number (p value 0.1), so we conclude that no parameters are found to be strongly correlated with RMS (5 kHz–20 MHz) density perturbations. Laufer (1964) found a strong dependence of tunnel noise on Mach number that was not maintained by the data presented in this paper; this is likely because of the more narrow range of conditions in Table 1 as compared to the conditions reported in Laufer (1964).

Contours of the power spectral density of a sample run are presented in time–frequency space as a spectrogram. The data indicate no clear trends in noise throughout the test time. This addresses the concern that weak non-steady waves or driver gas contamination (Sudani and Hornung 1998) may manifest themselves during the test time as trends in noise. Power spectral density estimates of each of the experiments are found to collapse upon each other when the streamwise disturbance convection velocity is used to eliminate the time scale. Furthermore, there is a strong dependence of the disturbance level on wavelength. When performing slender-body hypervelocity boundary-layer instability experiments in the T5 reflected-shock tunnel, the most strongly amplified wavelength is 2–4 mm. Per the described data processing routine with the focusing laser differential interferometer, if the disturbance band of interest is 700 μm–10 mm, then the tunnel noise is measured to be 0.5 % within this band.

Acknowledgments The authors would like to thank Bahram Valiferdowsi and Joe Jewell for help running T5, Ross Wagnild for help with the program to compute the run conditions, and Ivett Leyva for her helpful comments and thoughts.

References

Balakumar P, Kegerise MA (2010) Receptivity of hypersonic boundary layers over straight and flared cones. In: Proceedings of 48th AIAA aerosciences meeting, AIAA-2010-1065, Orlando, FL. doi:10.2514/6.2010-1065

Blanchard A, Lachowicz J, Wilkinson S (1996) Performance of the NASA-Langley Mach 6 Quiet Wind Tunnel. AIAA J 35(1):23–28. doi:10.2514/6.1996-441

Bounitch A, Lewis DR, Lafferty JF (2011) Improved measurements of tunnel noise pressure fluctuations in the AEDC hypervelocity wind tunnel no. 9. In: Proceedings of 49th AIAA aerospace sciences meeting including the new horizons forum and aerospace exposition, AIAA-2011-1200, Orlando, Florida. doi:10.2514/6.2011-1200

Browne S, Ziegler J, Shepherd JE (2006) Numerical solution methods for shock and detonation jump conditions. GALCIT—FM2006-006

Bushnell D (1990) Notes on initial disturbance fields for the transition problem. In: Hussaini M, Voigt R (eds) Instability and transition, ICASE/NASA LaRC series, Springer, Berlin, pp 217–232. doi:10.1007/978-1-4612-3430-2-28

Candler GV (2005) Hypersonic nozzle analysis using an excluded volume equation of state. In: Proceedings of 38th AIAA thermophysics conference, AIAA-2005-5202, Toronto, ON. doi:10.2514/6.2005-5202

Catrisa S, Aupoix B (2000) Density corrections for turbulence models. Aerosp Sci Technol 4(1):1–11

Coleman HW, Steele WG (1999) Experimentation and uncertainty analysis for engineers, 2nd edn. Wiley, New York

Draper NR, Smith H (1998) Applied regression analysis. Wiley-Interscience, London

Fedorov A (2003) Receptivity of a high-speed boundary layer to acoustic disturbances. J Fluid Mech 491:101–129. doi:10.1017/S0022112003005263

Fedorov A (2011) Transition and stability of high-speed boundary layers. Annu Rev Fluid Mech 43:79–95. doi:10.1146/annurev-fluid-122109-160750

Ffowcs-Williams JE, Maidanik G (1965) The mach wave field radiated by supersonic turbulent shear flows. J Fluid Mech 21(4):641–657. doi:10.1017/S0022112065000393

Fujii K, Shoichi T, Tadao K, Noriaki H (2013) Oscillation of bow-shock waves at hypersonic speeds. In: Proceedings of 43rd AIAA fluid dynamics conference, AIAA-2013-3103, Orlando, FL. doi:10.2514/6.2013-3103

Goodwin DG (2003) An open-source, extensible software suite for CVD process simulation. In: Allendorf M, Maury F, Teyssandier F (eds) Proceedings of CVD XVI and EuroCVD fourteen, pp 155–162

Gordon S, McBride B (1999) Thermodynamic data to 20,000 K for monatomic gases. NASA TP-1999-208523

Hofferth JW, Humble RA, Floryan DC, Saric WS (2013) High-bandwidth optical measurements of the second-mode instability in a Mach 6 quiet tunnel. In: Proceedings of 51st AIAA aerospace sciences meeting including the new horizons forum and aerospace exposition, AIAA 2013-0378, Grapevine, TX. doi:10.2514/6.2013-378

Hornung HG (1992) Performance data of the new free-piston shock tunnel at GALCIT. In: Proceedings of 17th AIAA aerospace ground testing conference, AIAA 1992-3943, Nashville, TN. doi:10.2514/6.1992-3943

Johnson HB (2000) Thermochemical interactions in hypersonic boundary layer stabity. Ph.D. thesis, University of Minnesota, Minnesota

Laufer J (1961) Aerodynamic noise in supersonic wind tunnels. J Aerosp Sci 28(9):685–692. doi:10.2514/8.9150

Laufer J (1964) Some statistical properties of the pressure field radiated by a turbulent boundary layer. Phys Fluids 7(8):1191–1197. doi:10.1063/1.1711360

Lee SS, Lele S, Moin P (1997) Interaction of isotropic turbulence with shock waves: effect of shock strength. J Fluid Mech 340:225–247. doi:10.1017/S0022112097005107

Maheash K, Lee S, Lele S, Moin P (1995) The interaction of an isotropic field of acoustic waves with a shock wave. J Fluid Mech 300:383–407. doi:10.1017/S0022112095003739

Marineau EC, Hornung HG (2010) Study of bow-shock wave unsteadiness in hypervelocity flow from reservoir fluctuations.

In: Proceedings of 48th AIAA aerospace sciences meeting including the New Horizons forum and aerospace exposition, AIAA-2010-382, Orlando, FL. doi:10.2514/6.2010-382

MathWorks (2013) Stepwisefit documentation page. http://www.mathworks.com

McBride B, Zehe MJ, Gordon S (2002) NASA Glenn coefficients for calculating thermodynamic properties of individual species. NASA TP-2002-211556

McGilvray M, Jacobs PA, Morgan RG, Gollan RJ, Jacobs CM (2009) Helmholtz resonance of pitot pressure measurements in impulsive hypersonic test facilities. AIAA 47(10):2430–2439. doi:10.2514/1.42543

Moore FK (1954) Unsteady oblique interaction of a shock wave with a plane disturbance. NACA TR-1165

Morkovin MV (1969) Critical evaluation of transition from laminar to turbulent shear layers with emphasis on hypersonically traveling bodies. AFFDL TR-68-149

Owen FK, Horstman CC, Stainback PC, Wagner RD (1975) Comparison of wind tunnel transition and freestream disturbance measurements. AIAA J 13(3):266–269. doi:10.2514/3.49691

Parziale NJ (2013) Slender-body hypervelocity boundary-layer instability. Ph.D. thesis, California Institute of Technology, California

Parziale NJ, Jewell JS, Shepherd JE, Hornung HG (2011) Shock tunnel noise measurement with resonantly enhanced focused Schlieren deflectometry. In: Proceedings of the 28th international symposium on shock waves, ISSW, Manchester

Parziale NJ, Shepherd JE, Hornung HG (2013) Differential interferometric measurement of instability in a hypervelocity boundary layer. AIAA J 51(3):750–754. doi:10.2514/1.J052013

Pate SR (1971) Measurements and correlations of transition Reynolds numbers on sharp slender cones at high speeds. AIAA J 9(6):1082–1090. doi:10.2514/3.49919

Pate SR (1971) Supersonic boundary-layer transition: effects of roughness and freestream disturbances. AIAA J 9(5):797–803. doi:10.2514/3.6278

Pate SR (1974) Comparison of NASA helium tunnel transition data with noise-transition correlation. AIAA J 12(11):1615. doi:10.2514/3.49564

Pate SR (1980) Effects of wind tunnel disturbances on boundary-layer transition with emphasis on radiated noise: a review. In: Proceedings of 11th aerodynamic testing conference, AIAA-1980-0431, Colorado Springs, CO. doi:10.2514/6.1980-0431

Pate SR, Schueler CJ (1969) Radiated aerodynamic noise effects on boundary-layer transition in supersonic and hypersonic wind tunnels. AIAA J 7(3):450–457. doi:10.2514/3.5128

Phillips OM (1960) On the generation of sound by supersonic turbulent shear layers. J Fluid Mech 9(1):1–28. doi:10.1017/S0022112060000888

Reshotko E (1976) Boundary-layer stability and transition. Annu Rev Fluid Mech 8:311–349. doi:10.1146/annurev.fl.08.010176.001523

Rufer S, Berridge D (2012) Pressure fluctuation measurements in the NASA Langley 20-Inch Mach 6 Wind Tunnel. In: Proceedings of 42nd AIAA fluid dynamics conference and exhibit, AIAA-2012-3262, New Orleans, LA. doi:10.2514/6.2012-3262

Saric WS, Reed HL, Kerschen EJ (2002) Boundary layer receptivity to freestream disturbances. Annu Rev Fluid Mech 34:291–319. doi:10.1146/annurev.fluid.34.082701.161921

Schneider SP (2001) Effects of high-speed tunnel noise on laminar–turbulent transition. J Spacecr Rockets 38(3):323–333. doi:10.2514/2.3705

Schneider SP (2004) Hypersonic laminar–turbulent transition on circular cones and scramjet forebodies. Prog Aerosp Sci 40(1–2):1–50. doi:10.1016/j.paerosci.2003.11.001

Schneider SP (2008) Development of hypersonic quiet tunnels. J Spacecr Rockets 45(4):641–664. doi:10.2514/1.34489

Siegman AE (1986) Lasers. University Science Books, Mill Valley

Smeets G (1972) Laser interferometer for high sensitivity measurements on transient phase objects. IEEE Trans Aerosp Electron Syst AES 8(2):186–190. doi:10.1109/TAES.1972.309488

Smeets G, George A (1973) Anwendungen des laser-differential interferometers in der gasdynamik. ISL-N 28/73, Also translated by Goetz as ADA-307459

Smith DR, Smits AJ (1993) Simultaneous measurement of velocity and temperature fluctuations in the boundary layer of a supersonic flow. Exp Thermal Fluid Sci 7(3):221–229. doi:10.1016/0894-1777(93)90005-4

Smits AJ, Hayakawa K, Muck KC (1983) Constant temperature hot-wire anemometer practice in supersonic flows. Exp Fluids 1(2):83–92. doi:10.1007/BF00266260

Spalart PR, Allmaras SR (1992) A One-equation turbulence model for aerodynamic flows. In: Proceedings of 30th AIAA aerospace sciences meeting and exhibit, AIAA 1992-439, Reno, NV. doi:10.2514/6.1992-439

Spina EF, McGinley CB (1994) Constant-temperature anemometry in hypersonic flow: critical issues and sample results. Exp Fluids 17(6):365–374. doi:10.1007/BF01877036

Stainback PC, Wagner RD (1972) A comparison of disturbance levels measured in hypersonic tunnels using hot-wires anemometer and a pitot pressure probe. In: Proceedings of 7th AIAA aerodynamic testing conference, AIAA-1972-1003, Palo Alto, CA. doi:10.2514/6.1972-1003

Sudani N, Hornung HG (1998) Gasdynamical detectors of driver gas contamination in a high-enthalpy shock tunnel. AIAA 36(3):313–319. doi:10.2514/2.383

Wagner RD Jr, Maddalon DV, Weinstein LM (1970) Influence of measured freestream disturbances on hypersonic boundary-layer transition. AIAA J 8(9):1664–1670. doi:10.2514/3.5962

Wagnild RM (2012) High enthalpy effects on two boundary layer disturbances in supersonic and hypersonic flow. Ph.D. thesis, University of Minnesota, Minnesota

Weiss J, Knauss H, Wagner S (2003) Experimental determination of the free-stream disturbance field in a short-duration supersonic wind tunnel. Exp Fluids 35(4):291–302. doi:10.1007/s00348-003-0623-z